

ICNMM2008-62323

SIMULATION-BASED ANALYSIS OF A BIOLOGICALLY-INSPIRED MICROPUMP WITH A ROTATING SPIRAL INSIDE A MICROCHANNEL

Mustafa Koz
Faculty of Engineering and Natural Sciences
Sabanci University, Istanbul, Turkey
mustafak@su.sabanciuniv.edu

Serhat Yesilyurt
Faculty of Engineering and Natural Sciences
Sabanci University, Istanbul, Turkey
syesilyurt@sabanciuniv.edu

ABSTRACT

Microorganisms such as bacteria use their rotating helical flagella for propulsion speeds up to tens of tail lengths per second. The mechanism can be utilized for controlled pumping of liquids in microchannels. In this study, we aim to analyze the effects of control parameters such as axial span between helical rounds (wavelength), angular velocity of rotations (frequency), and the radius of the helix (amplitude) on the maximum time-averaged flow rate, maximum head, rate of energy transfer, and efficiency of the micropump. The analysis is based on simulations obtained from the three-dimensional time-dependent numerical model of the flow induced by the rotating spiral inside a rectangular-prism channel. The flow is governed by Navier-Stokes equations subject to continuity in time-varying domain due to moving boundaries of the spiral. Numerical solutions are obtained using a commercial finite-element package which uses arbitrary Lagrangian-Eulerian method for mesh deformations. Results are compared with asymptotic results obtained from the resistive-force-theory available in the literature.

INTRODUCTION

Micropumps have a large variety of application areas, such as cooling of electronic components, medical diagnosis and drug delivery, lab-on-a-chip devices used in biology and chemistry, and space exploration [1]. For these particular applications, large scale pumps cannot be geometrically scaled down for microfluidic applications due to exchanged roles of viscous and inertial forces in the micro and macroscales. Namely, viscous effects are more dominant than inertial forces in microscales. A dramatic analogy is provided by Purcell: conditions of microorganisms swimming in water are identical to those of humans swimming in tar filled pools [2].

Typical micropumps depend either on mechanical displacements or electric fields. The latter may become problematic for fluids sensitive to electric fields [1]. In this context, biologically inspired actuation mechanisms can be viable alternatives for enabling of microflows.

The micropump analyzed here is inspired from microorganisms such as Ecoli bacteria which have rotating helical flagella to propel themselves. The magnitude of the propulsion is up to the tens of tail lengths per second [3]. A helical rod with fixed ends placed inside a rectangular channel and rotated around the axis of the rod. The flow created by the rotation of helical rods is analyzed by several authors [4-6]. Based on the resistive force [7] and slender body [8] theories, the swimming speed of the organism is obtained by Lighthill [9], and Behkam and Sitti [10].

In this work, we present simulation-based experiments with the micropump that consists of a rotating helical rod placed in a rectangular-prism-microchannel as shown in Fig. 1. In this system, as the spiral rotates inside the microchannel, a point on the spiral's boundary moves on the yz-plane only for a given x. Shearing action enabled by the spiral, in turn, results in a net flow in the x-direction. As the shearing action between the tail and the fluid gets stronger, the flow in the x-direction becomes stronger. In this model, the flow is governed by three-dimensional time-dependent Navier-Stokes equation in a moving domain as opposed to assuming that Stokes equations suffice as presented in our earlier work [11]. Furthermore, parametric dependence of the efficiency and pressure head of the micropump on the wavelength, frequency and amplitude is presented here.

NOMENCLATURE

Symbol	Description
Latin Letters	
<i>A</i>	Area
<i>B</i>	Wave Amplitude
I	Identity Matrix
<i>L</i>	Rod Length
<i>P</i>	Liquid Pressure
<i>Q</i>	Flow Rate
<i>U</i>	Speed of the Microswimmer
U	Fluid Velocity Vector
<i>a</i>	Radius of The Swimmer Head
d	Displacement Vector
<i>f</i>	Rotation Frequency [Hz]

h	Channel Width and Height
n	Power In Amplitude Function
\mathbf{n}	Outward Normal of Inlet or Outlet
r	Radius of The Rod
t	Spatial Time
\mathbf{u}	Mesh Velocity Vector
u,v,w	Velocity Components
x,y,z	Spatial Coordinates
\mathbf{x}	Coordinate of Rod Surface

Functions and Groups

B	Amplitude Function
C	Coefficient of Resistance
Re	Reynolds Number
g	Factor of Power

Greek Letters

Ω	Domain Occupied by Fluid Inside
Π	Rate of Energy Transferred to Fluid
Σ	Stress Tensor
β	Angel Between Rod and Plane of Rotation
η	Rate of Energy
λ	Wave Length
μ	Dynamic Viscosity of Fluid
ω	Angular Velocity [Radians]
ρ	Liquid Density

Subscripts and Superscripts

T	Transpose
*	Reference Case Parameter
0	Maximum Possible Value
av	Average
$helix$	Helix Parameter
int	Initial Coordinates of Rod Surface
l	Tangential to Rod Surface
m	Mesh Parameter
max	Maximum Value
mid	Midpoint of the Rod
n	Normal to Rod Surface
r	Random
rod	Rod Parameter
x,y,z	Direction Parameters

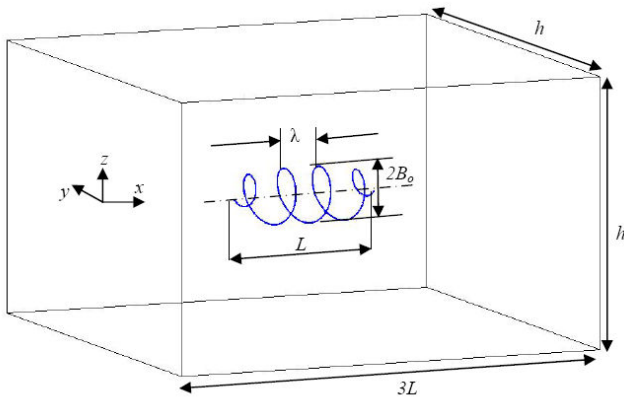


Figure 1: Layout of the channel with a spiral placed inside as used in simulations

METHODOLOGY

The rectangular prism channel that is shown in Fig. 1 has three times the axial length of the helix inside. Inlet and outlet regions provide sufficient manifolds for the flow recovery. The helical rod is defined by two variables which are wavelength, λ and amplitude, B_0 . When the helix rotates, the wave formed by the rod travels in the negative x-direction. Coordinate system is at the middle point of the outlet and x-vector coincides with the rotation axis of the helix. The helix in the channel is created from a deformed straight rod which has a radius of r_0 . The deformation is on the yz-plane and depends on the x-position and time, t , as follows:

$$\mathbf{d}_{rod}(x,t) = \begin{bmatrix} x_{rod} \\ y_{rod} \\ z_{rod} \end{bmatrix} = B(x) \begin{bmatrix} 0 \\ \sin(2\pi x/\lambda + \omega t) \\ \cos(2\pi x/\lambda + \omega t) \end{bmatrix}. \quad (1)$$

In (1), the function $B(x)$ is used to make sure the ends of the helix do not move in the y-z plane, and the maximum amplitude takes place in the middle of the rod as follows:

$$B(x) = B_0 \left(1 - \left[\frac{x - x_{mid}}{L/2} \right]^n \right). \quad (2)$$

In (2) B_0 is the maximum amplitude, parameter n adjusts amplitude distribution among the helix and x_{mid} is the x-coordinate of the midpoint of the rod.

Flow in the microchannel is time-dependent, three-dimensional, incompressible and governed by unsteady Navier-Stokes equation in a deforming domain:

$$\rho \left(\frac{\partial \mathbf{U}}{\partial t} + (\mathbf{U} - \mathbf{u}_m) \cdot \nabla \mathbf{U} \right) = -\nabla P + \mu \nabla^2 \mathbf{U} \text{ in } \Omega(t); \quad (3)$$

subject to continuity,

$$\nabla \cdot \mathbf{U} = 0 \text{ in } \Omega(t). \quad (4)$$

In equation (3), \mathbf{U} is the velocity field of the flow, P is pressure, ρ is the density and μ is the viscosity of the fluid, and \mathbf{u}_m is the velocity of the deforming domain with respect to initial domain which corresponds to the channel with an undeformed straight rod.

$$\mathbf{u}_m(\mathbf{x}_{\Omega(t)}, t) \equiv \frac{d\mathbf{x}_{\Omega(t)}}{dt} \Big|_{\Omega(0)}. \quad (5)$$

In effect, the velocity of the deforming domain reflects the Lagrangian definition of the flow, and corresponds to the moving mesh velocity in the finite-element representation [12].

Equations (3) and (4) are subject to no-slip boundary conditions at the channel walls and the surface of the helical

rod. Thus, channel wall surfaces have zero velocity while the velocity at the helix surface is specified using Equation (1):

$$\mathbf{U}(\mathbf{x}_{rod}, t) = \mathbf{v}_{rod}(x, t) = \begin{bmatrix} \dot{x}_{rod} \\ \dot{y}_{rod} \\ \dot{z}_{rod} \end{bmatrix} = \omega B(x) \begin{bmatrix} 0 \\ \cos(2\pi x/\lambda + \omega t) \\ -\sin(2\pi x/\lambda + \omega t) \end{bmatrix} \quad (6)$$

In (6), \mathbf{x}_{rod} represents the surface coordinate vector of the helix.

$$\mathbf{x}_{rod} = \mathbf{x}_{int} + \mathbf{d}_{rod}, \quad (7)$$

where \mathbf{d}_{rod} is given in (1) and \mathbf{x}_{int} is the coordinate vector of the undeformed straight rod.

Inlet pressure is always kept zero:

$$[-P\mathbf{I}] \cdot \mathbf{n} \Big|_{x=3L, y, z, t} = 0. \quad (8)$$

However, the outlet pressure varies in simulations.

$$[-P\mathbf{I}] \cdot \mathbf{n} \Big|_{x=0, y, z, t} = P_{out}, \quad (9)$$

P_{out} is set to zero for the maximum flow rate simulations, and non-zero values to find the maximum pressure load.

Flow is initially at rest:

$$\mathbf{U}(x, y, z, 0) = [0 \quad 0 \quad 0]^T \quad (10)$$

In order to avoid infinite accelerations in the flow field at $t=0$, the velocity of the rotating helix is multiplied with a time-dependent ramp function which creates a smooth transition in the first third of the period.

Instantaneous flow rate, $Q(t)$, is obtained from the integration of the x-component of the velocity over the inlet surface, i.e.

$$Q(t) = \int_{outlet} \mathbf{U}(x, y, z, t) \cdot \mathbf{n} dA \quad (11)$$

Time-averaged flow rate, Q_{av} , is obtained from the time-integration of $Q(t)$ over the last two periods of the simulation:

$$Q_{av} = \frac{1}{t_1 - t_0} \int_{t_0}^{t_1} Q(t) dt \quad (12)$$

Instantaneous rate of energy transferred from helix to fluid is calculated by the integration of the inner product of stress tensor and the velocity vector over the surface of the helical rod:

$$\Pi(t) = \int_{Rod \ surface} \Sigma \cdot \mathbf{v}_{rod} dA = \int_{Rod \ surface} [\Sigma_y \dot{y}_{rod} + \Sigma_z \dot{z}_{rod}] dA \quad (13)$$

where, Σ_y and Σ_z are the y and z-components of the stress tensor respectively [12], and given by:

$$\Sigma_y = \mu \left(\frac{\partial u}{\partial y} + \frac{\partial v}{\partial x} \right) n_x + \left(2\mu \frac{\partial v}{\partial y} - P \right) n_y + \mu \left(\frac{\partial v}{\partial z} + \frac{\partial w}{\partial y} \right) n_z \quad (14)$$

$$\Sigma_z = \mu \left(\frac{\partial u}{\partial z} + \frac{\partial w}{\partial x} \right) n_x + \mu \left(\frac{\partial v}{\partial z} + \frac{\partial w}{\partial y} \right) n_y + \left(2\mu \frac{\partial w}{\partial z} - P \right) n_z \quad (15)$$

Surface normal vector of the helical rod has three components x,y and z direction that are n_x , n_y , and n_z respectively. Equation (12) gives Π_{av} if the term $Q(t)$ is exchanged with $\Pi(t)$.

Hydraulic efficiency, η is the ratio of the hydraulic power of the fluid, which does work against a specific pressure difference, to the rate of work done on the fluid by the rotation of the helix against the shear:

$$\eta = 100 \frac{\Delta P Q_{av}}{\Pi_{av}} \quad (16)$$

In (16) pressure difference, ΔP and time-averaged flow rate are inversely dependent to each other. However, Π_{av} is typically independent of ΔP and Q_{av} .

RESULTS

Geometric parameters, properties and base case operating conditions that are used in the simulations are listed in Table 1. Water is selected as the working fluid. Along the operating conditions of micropump and geometric configuration of the helical rod, a reference case parameter set is selected as: $f=1\text{Hz}$, $B_0=10\mu\text{m}$ and $\lambda=320\mu\text{m}$.

Numerical solution of Navier-Stokes equation is obtained by using a commercial finite-element software, COMSOL. The micropump is modeled with 18406 quadratic Lagrange finite-elements which result in 84781 degrees-of-freedom. Each simulation takes about 5 hours on average on a double dual-core, 3.7GHz, Xeon processor workstation with 16 GB RAM and running 64-bit SUSE 10.2 Linux operating system. Linear system of equations is solved by using the PARDISO solver and the fifth degree interpolation polynomial in the backward-differentiation time-stepping method [12]. Relative and absolute tolerance values are set to 10^{-4} and 10^{-5} respectively. Error estimation strategy excludes algebraic variables.

In Figure 2, arrows represent the fluid flow and the color distribution corresponds to the pressure distribution on the channel walls. Arrows are normalized to show only the direction of the flow. There is a steady flow at the inlet and the outlet with a typical parabolic laminar profile. However, near the rod, velocity arrows are larger on the yz-plane which is normal to flow direction along with a strong circulation near the rod. Direction of the arrows indicates the flow from high to low pressure regions for which the pressure variation corresponds to between -1.757 and 1.274 mPa.

Table 1: Geometric variables of the channel, properties of the fluid (water), and base case conditions of the helical rod.

Quantity	Value
Channel width and height, h	200 μm
Channel length, $3L$	960 μm
Rod length, L	320 μm
Radius of the rod, r_0	10 μm
Viscosity of the fluid, μ	$1.12 \times 10^{-3} \text{ kg m}^{-1} \text{ s}^{-1}$
Density of the fluid, ρ	10^3 kg m^{-3}
Frequency (reference case), f^*	1 Hz
Amplitude (reference case), B_0^*	10 μm
Wavelength (reference case), λ^*	320 μm
Power in amplitude function, n	6

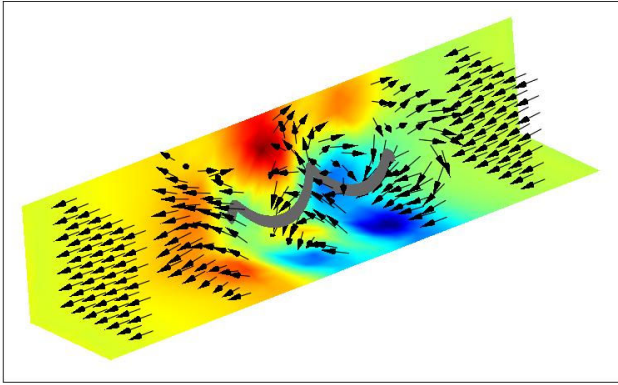


Figure 2: Velocity vectors and pressure distribution for the case ($f = 1\text{Hz}$, $B_0 = 10 \mu\text{m}$ and $\lambda=160 \mu\text{m}$) at $t = 3 \text{s}$; for clarity axes are removed.

Instantaneous inlet-averaged flow rate for the reference case is depicted in Fig. 3 for the last two thirds of the total simulation time. Time-averaged flow rate is $1.87 \times 10^{-3} \mu\text{l}/\text{min}$, and corresponds to the Reynolds number of 6.7×10^{-4} . Despite the steadiness of the local flow, a periodic variation of the flow rate is observed with respect to time. The figure is obtained from a simulation which uses a finer mesh and smaller convergence criterion than normally used. However, in Fig. 3 we cannot claim that the results are numerical noise free. On the other hand, temporal variations from the average flow rate are more pronounced for large wavelengths. In Figures 4 and 5, average flow rate is shown as a function of time for wavelengths of $80 \mu\text{m}$ and $640 \mu\text{m}$ respectively. Similar behavior is observed in the numerical simulations of the micropump that is actuated by travelling-plane-wave deformations [13].

Time-averaged flow rates are plotted in Figs. 6, 7 and 8 to show the dependency of the flow rate on frequency, amplitude and wavelength respectively. In order to make a point-to-point comparison with analytical solutions presented by Behkam and Sitti [10], each plot shows both numerical and analytical results. Since the analytical solutions are derived for the speed of the microswimmer, for a convenient comparison between these two solutions, both flow rate and swimming speed values are normalized by the reference case outputs of each method. Normalizing swimming speed for the base case is obtained as $4.99 \mu\text{m}/\text{s}$.

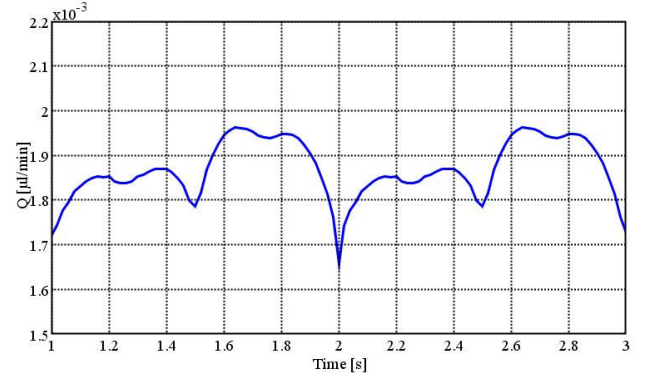


Figure 3: Instantaneous flow rate of the reference case ($f=1\text{Hz}$, $B_0 = 10 \mu\text{m}$ and $\lambda = 320 \mu\text{m}$).

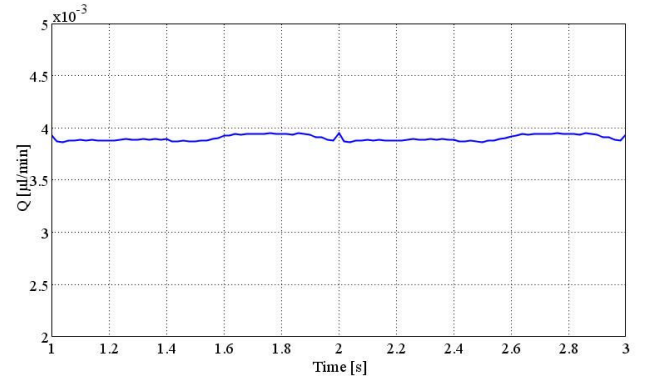


Figure 4: Instantaneous flow rate of the case ($f = 1\text{Hz}$, $B_0 = 10 \mu\text{m}$ and $\lambda = 80 \mu\text{m}$).

The speed of a microswimmer is calculated by Behkam and Sitti based on the resistive force theory [10,13]

$$U = \frac{m\lambda V_0 \sin \beta \cos \beta (C_{n,helix} - C_{l,helix})}{n\lambda (C_{n,helix} \sin^2 \beta + C_{l,helix} - C_{l,helix} \sin^2 \beta) + 6\pi\mu a \cos \beta} \quad (17)$$

where $C_{n,helix}$ and $C_{l,helix}$ are coefficients of resistance determined by the resistive force theory, and are functions of the wavelength, λ , radius of the rod, r_0 and viscosity of the fluid, μ . In (17), β is the angle between the helix and the plane of rotation. The value of β is calculated by $\beta = \tan^{-1}(2\pi/\lambda B_0)$.

Tangential velocity of the helix is expressed as $V_\theta = \omega B_0$ and a is the radius of the swimmer's head which is taken equal to $r_0 = 10 \mu\text{m}$.

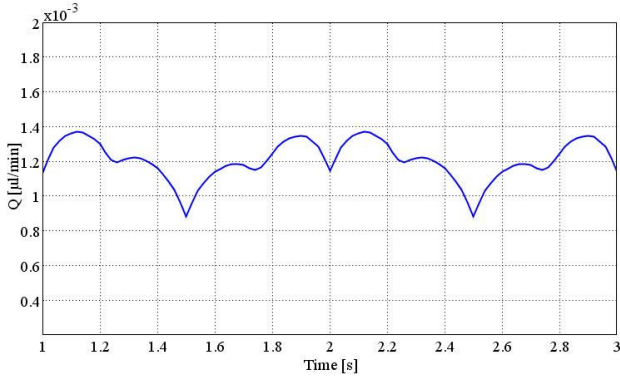


Figure 5: Instantaneous flow rate of the case ($f = 1\text{Hz}$, $B_0 = 10 \mu\text{m}$ and $\lambda = 640 \mu\text{m}$).

Numerical and analytical solutions to frequency dependency of the flow are indistinguishable in Fig. 6. They both show linear variation with frequency.

Figure 7 shows quadratic variation of normalized flow rate and normalized velocity of the swimmer with amplitude for small amplitudes. The results overlap with a small deviation which stems from the different extensibility conditions of the helical rod for numerical and analytical models. In our model, total length of the helix changes with the amplitude, whereas in analytical solutions total length of the swimmer tail remains the same for all amplitude values. Hence, in Fig. 5 for amplitude values higher than the reference case, simulations show higher flow rates than they are calculated by analytical approach. Similarly, for a smaller amplitude value, like $1 \mu\text{m}$, than the reference case value, $10 \mu\text{m}$, the flow rate is calculated smaller than the analytical approach.

Figure 8 shows the variation of normalized flow rate and normalized velocity of the swimmer with wavelength. According to simulation results the average flow rate and swimming speed of the microorganism decrease with increasing wavelength. For the varying rate of decrease of the flow rate with respect to the wavelength, one can claim the presence of end effects of the rectangular channel in which the helical rod lies.

Figure 9 to 11 show the effect of control parameters, f , B_0 and λ on the rate of energy transferred to the working fluid from the motion of the helical rod. According to the analysis presented by Lighthill [9], the rate of energy transfer to the working fluid is proportional to the square of the swimmer's speed with a factor that depends on amplitude, wavelength and the length of the helical rod:

$$\Pi_{av} \propto U^2 g(B_0, \lambda, L) \quad (18)$$

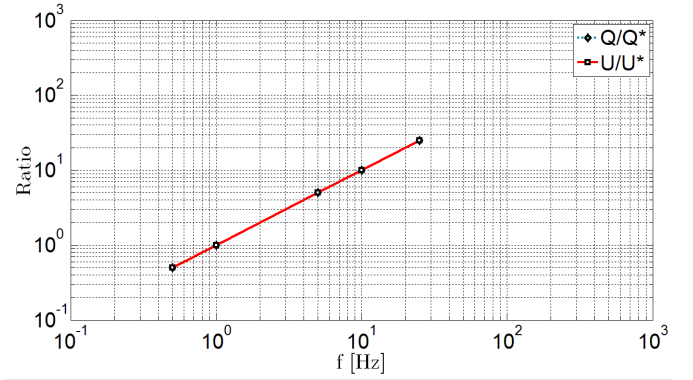


Figure 6: The effect of the frequency on the normalized flow rate and the normalized velocity of the swimmer.

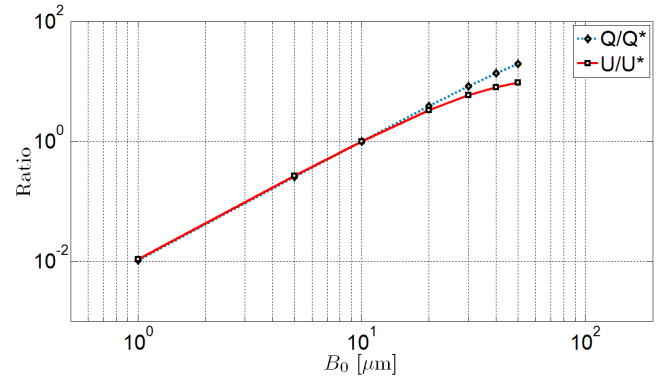


Figure 7: The effect of the amplitude on the normalized flow rate and the normalized velocity of the swimmer.

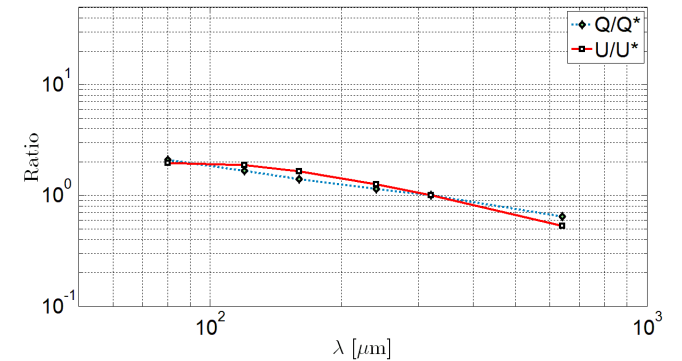


Figure 8: The effect of the wavelength on the normalized flow rate and the normalized velocity of the swimmer.

Figure 9 demonstrates quadratic dependence of rate of energy transfer (i.e. hydraulic power) on frequency. Since the flow rate and the speed of the swimmer are linearly proportional to the frequency (in Fig. 6 and Eq. (17)) and according to (18), it is expected to have quadratic dependence between the hydraulic power and the frequency.

According to Fig. 10, amplitude has a quadratic effect on the hydraulic power. The Lighthill's derivation does not provide a simple one-to-one comparison between the conditions of the swimmer and the micropump, but according to Fig. 7 and Eq. (18), one can expect the rate of energy transfer as proportional to the square of the amplitude.

Wavelength does not have a significant effect on rate of energy transfer from the helical rod to the flow as shown in Fig. 11.

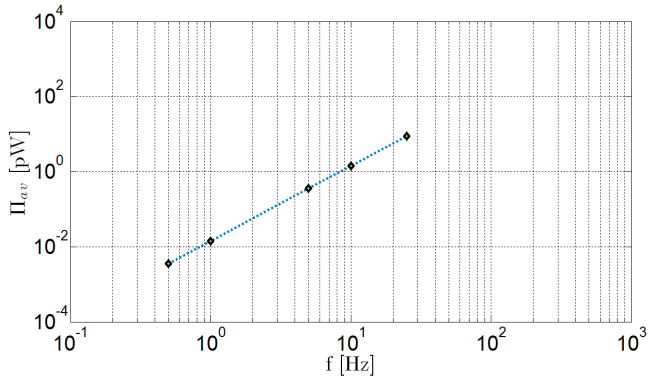


Figure 9: Time-averaged rate of energy transferred to the fluid as the function of frequency.

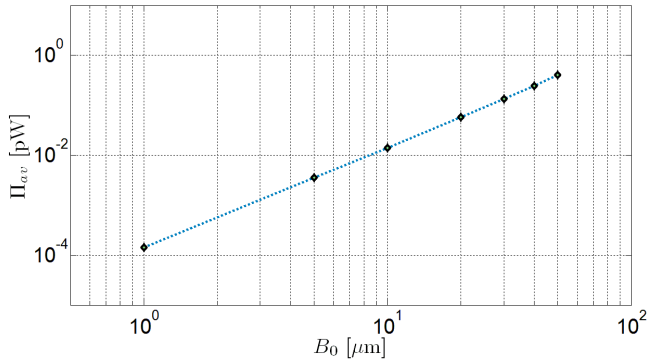


Figure 10: Time-averaged rate of energy transferred to the fluid as the function of amplitude.

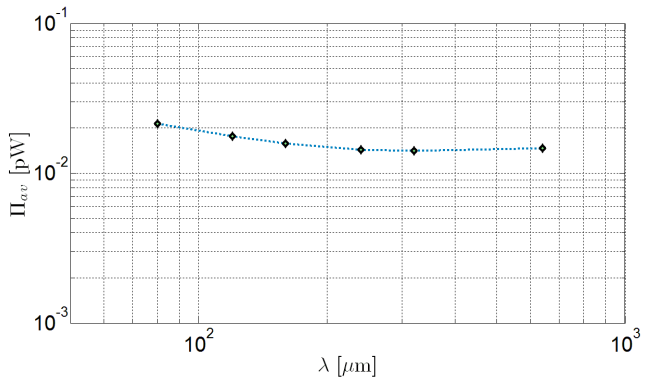


Figure 11: Time-averaged rate of energy transferred to the fluid as the function of wavelength.

In order to find the maximum pressure head that each micropump configuration can balance with a non-zero flow rate, micropump is operated against a number of pressure heads. Since the pump has characteristics of a viscous pump, the variation of the pressure with the flow rate is linear. Thus the maximum pressure head, which can be sustained by the pump, is obtained from an extrapolation.

Figures 12 to 14 show the variation of the maximum pressure head, ΔP_{max} with respect to frequency, f , amplitude, B_0 and wavelength, λ respectively. Frequency and amplitude has a linear effect whereas the wavelength affects the pressure head inversely.

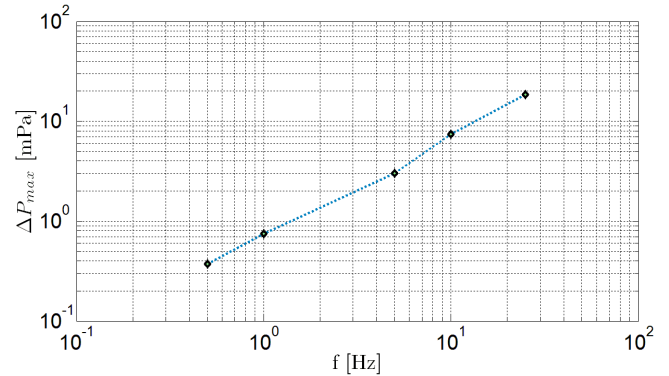


Figure 12: Maximum pressure load as a function of frequency.

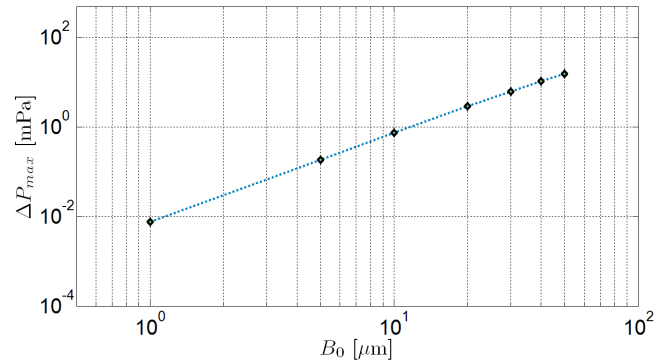


Figure 13: Maximum pressure load as a function of amplitude.

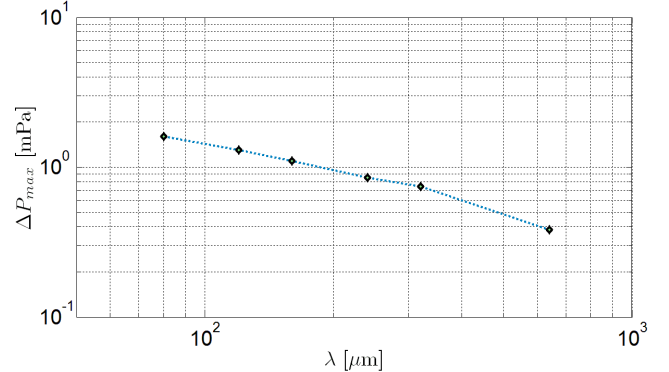


Figure 14: Maximum pressure load as a function of wavelength.

Lastly, using the results for the maximum flow rate (for zero pressure head) and the maximum pressure head, we determine the variation of the hydraulic efficiency of the pump with respect to frequency, amplitude and the wavelength. In particular, the maximum efficiency of the micropump, η_{max} is obtained from:

$$\eta_{max} = \frac{P_{max} Q_{max}}{\Pi_{av}} \quad (19)$$

Parametric variation of the efficiency is shown in Figures 15 to 17 frequency, amplitude and wavelength respectively. Simulation results show that frequency has no effect on efficiency (Fig. 15).

Efficiency has a quadratic dependence on the amplitude for small values. However, as the amplitude increases, the proportionality transforms into a linear one. Figure 16 shows this behavior for the complete range of amplitude parameters.

According to Fig. 17, the efficiency of the micropump decreases with increasing wavelength due to combined effects of decreasing flow rate and pressure and unchanging rate of energy transfer from the tail to the fluid as formulated in (19).

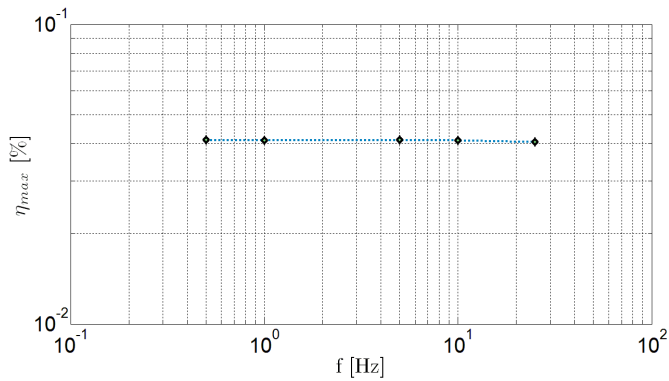


Figure 15: Maximum efficiency as a function of frequency.

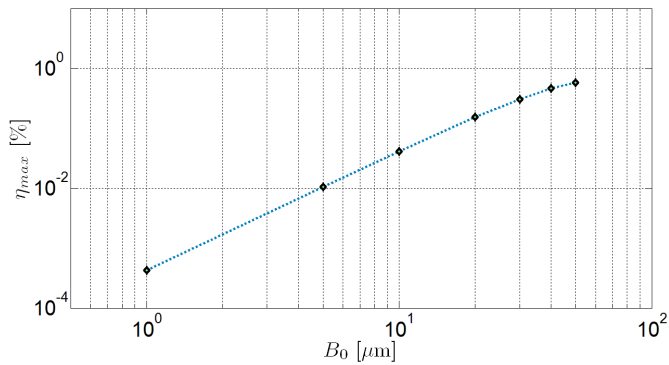


Figure 16: Maximum efficiency as a function of amplitude.

CONCLUSION

A biologically inspired micropump is parametrically analyzed by means of simulation experiments. The pump is based on the rotation of a helical rod inside a rectangular duct akin to flagellar motion of microorganisms. To model the flow induced by the rotational motion of the helical rod inside the channel, three-dimensional time-dependent Navier Stokes equations are used in a deforming domain using a commercial

finite-element package, COMSOL, which invokes the Arbitrary Lagrangian Eulerian method.

Four criteria are used to analyze the performance of the micropump: maximum flow rate, Q_{max} , rate of energy transfer, Π_{av} , maximum pressure load, ΔP_{max} and maximum hydraulic efficiency, η_{max} . Results are compared with the analytical work on microswimmers reported in the literature, most of which show similar findings to what is reported here.

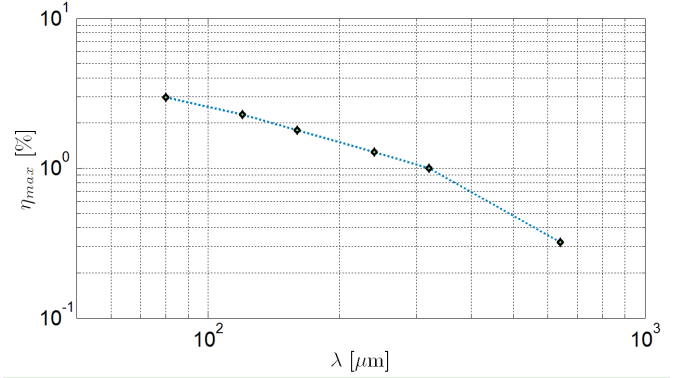


Figure 17: Maximum efficiency as a function of wavelength.

According to simulation results:

1. Frequency has a linear effect on Q_{max} and ΔP_{max} while it has a quadratic effect on Π_{av} . As a result, η_{max} does not vary with frequency.
2. Amplitude has a quadratic effect on Q_{max} , ΔP_{max} , Π_{av} and, thus, η_{max} , for small values. For larger amplitudes, the effect becomes linear.
3. Wavelength has an inverse effect on the flowrate and the pressure head, and does not have a significant effect on Π_{av} and η_{max} .

ACKNOWLEDGMENTS

We kindly acknowledge the partial support for this work from the Sabanci University Internal Grant Program (contract number IACF06-00418).

REFERENCES

- [1] Laser, D.J.; Santiago, J.G.; A review of micropumps; *J. Micromech. Microeng.*, **14**, (2004) R35-R64.
- [2] Purcell, E.M.; Life at Low Reynolds Number; *American Journal of Physics*, Vol. 45, No 1 (1977) 3-11.
- [3] Brennen, C.; Winet, H.; Fluid Mechanics of Propulsion by Cilia and Flagella; *Ann. Rev. Fluid Mech.* 9 (1977) 339-98.
- [4] Gray, J.; Ciliary Movement; *Camb. Un. Press.* (1928).
- [5] Sir Lighthill, J.; Mathematical Biofluidynamics; *Society for Industrial and Applied Mathematics* (1975).
- [6] Sir Taylor, G.I.; Analysis of the Swimming of Microscopic Organisms; *Proc Roy Soc., A* **209** (1951) 447-61
- [7] Sir Taylor, G.I.; Motion of axisymmetric bodies in viscous fluids; in *Problems of Hydrodynamics and Continuum Mechanics*, SIAM (1969) 718-24
- [8] Gray, J.; Hancock, G. J.; Propulsion of Sea-Urchin Spermatozoa; *J. Exp. Biol.* **32** (1955) 802-814

- [9] Sir Lighthill. J.; Flagellar hydrodynamics: The von Neumann Lecture, 1975; *SIAM Review* 18(2) 1976 161-230.
- [10] Behkam, B.; Sitti, M.; Design methodology for biomimetic propulsion of miniature swimming robots; *Journal of dynamic systems, measurement and control*, **128** 2006 36-43.
- [11] Koz, M.; Yesilyurt, S.; Simulations of microflows induced by rotation of spirals in microchannels, *Proceedings of the SPIE, Microfluidics, BioMEMS, and Medical Microsystems VI*, eds. Wang, W. and Vauchier, C., Volume 6886 2008.
- [12] COMSOL AB.; Comsol Multiphysics Modelling Guide, 2007.
- [13] Tabak, A.F.; Yesilyurt, S.; Simulation-based analysis of flow due to traveling-plane-wave deformations on elastic thin-film actuators in micropumps, *Microfluidics and Nanofluidics*, DOI:10.1007/s10404-007-0207y.
- [14] Hancock, G.J.; The self-propulsion of microscopic organisms through liquids, *Proceedings of the Royal Society of London Series A, Mathematical and Physical Sciences*, **217** 1953 96-121.